iScience

CellPress
OPEN ACCESS

Article

EBAG9-deficient mice display decreased bone mineral density with suppressed autophagy

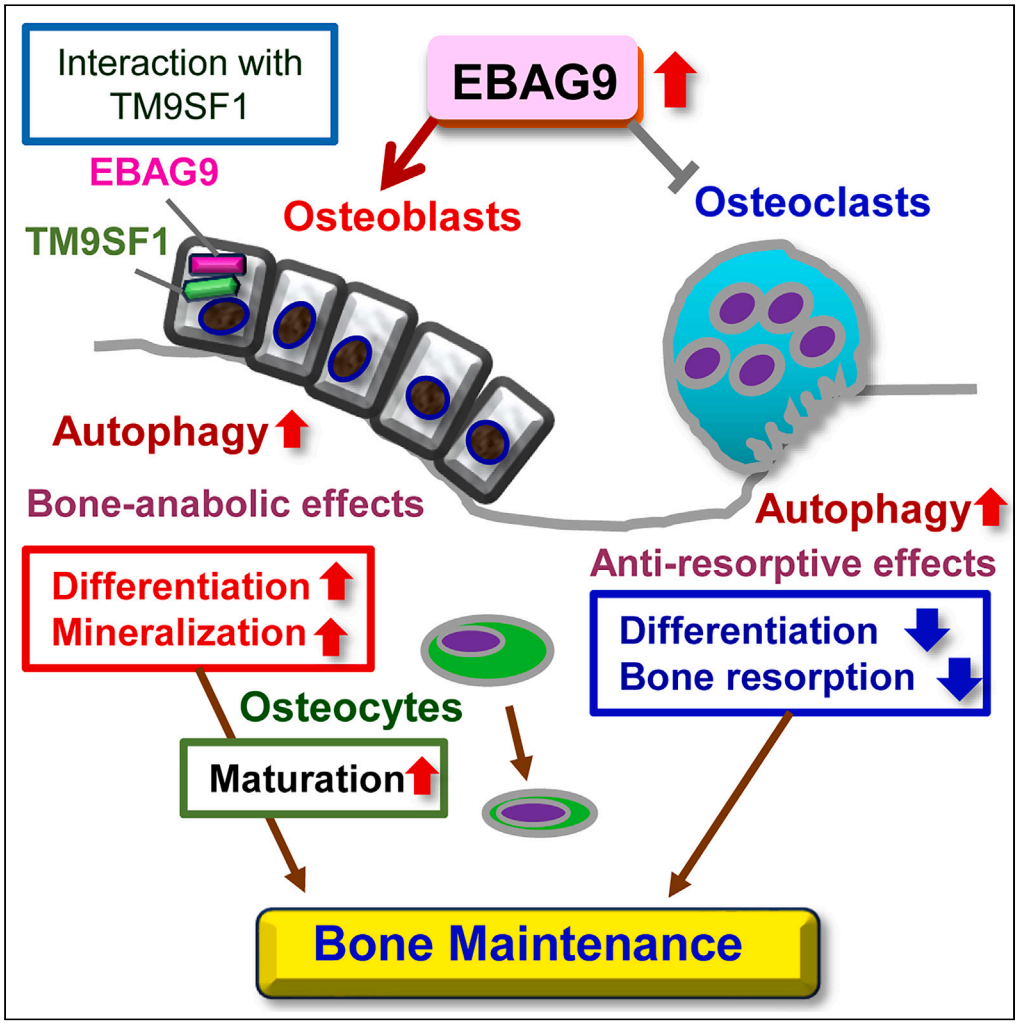

Kotaro Azuma, Kazuhiro Ikeda, Sachiko Shiba, ..., Norio Amizuka, Shinya Tanaka, Satoshi Inoue

sinoue@tmig.or.jp

Highlights

Ebag9-knockout mice displayed fragile bone with suppressed bone formation

Serum turnover markers showed enhanced bone resorption in *Ebag9*-knockout mice

EBAG9 promotes autophagy in both osteoblastic and osteoclastic lineages

EBAG9-interactor TM9SF1 affects differentiation and autophagy of osteoblastic cells

Azuma et al., iScience 27, 108871
February 16, 2024
https://doi.org/10.1016/j.isci.2024.108871

iScience

CellPress
OPEN ACCESS

Article

EBAG9-deficient mice display decreased bone mineral density with suppressed autophagy

Kotaro Azuma,[1,2] Kazuhiro Ikeda,[3] Sachiko Shiba,[3] Wataru Sato,[3] Kuniko Horie,[3] Tomoka Hasegawa,[4] Norio Amizuka,[4] Shinya Tanaka,[5,6] and Satoshi Inoue[1,3,7,*]

SUMMARY

Estrogen receptor-binding fragment associated antigen 9 (EBAG9) exerts tumor-promoting effects by inducing immune escape. We focused on the physiological functions of EBAG9 by investigating the bone phenotypes of *Ebag9*-knockout mice. Female *Ebag9*-knockout mice have fragile bones with lower bone mineral density (BMD) compared with wild-type mice. Histomorphometric analyses demonstrated that lower BMD was mainly caused by decreased bone formation. Serum bone turnover markers showed that enhanced bone resorption also contributed to this phenotype. We revealed that EBAG9 promoted autophagy in both osteoblastic and osteoclastic lineages. In addition, the knockdown of *Tm9sf1*, a gene encoding a protein that functionally interacts with EBAG9, suppressed autophagy and osteoblastic differentiation of the murine preosteoblastic cell line MC3T3-E1. Finally, overexpression of TM9SF1 rescued the suppression of autophagy caused by the silencing of *Ebag9*. These results suggest that EBAG9 plays a physiological role in bone maintenance by promoting autophagy together with its interactor TM9SF1.

INTRODUCTION

Estrogen receptor-binding fragment associated antigen 9 (EBAG9) was originally cloned by screening genes with an associated CpG island containing a typical estrogen-responsive element using a cDNA library of the breast cancer cell line, MCF-7.[1] We demonstrated that mRNA of *Ebag9* was induced by estrogen in MCF-7 cells. In the year following our publication, the protein encoded by the same gene was reported as a receptor-binding cancer antigen expressed on SiSo cells (RCAS1).[2] At the beginning, RCAS1 was thought to be a tumor antigen expressed on the cell surface and to play a role in helping evade immune surveillance. Later, EBAG9 was shown to mainly localize to the Golgi apparatus and affect the maturation of sugar chains on the cell surface.[3–5]

EBAG9 has been shown to be a poor prognostic factor for several cancers. Stronger immunoreactivity of EBAG9 protein in tumor tissues was associated with poor prognosis in patients with prostate cancer,[6] renal cancer,[7] bladder cancer,[8] testicular cancer,[9] and breast cancer.[10] Furthermore, EBAG9 expression in immune cells could be also responsible for the poor prognosis, as well as in tumor cells. This was suggested by studies using *Ebag9*-knockout mice in which cytotoxic T lymphocytes were activated.[11,12] One of these studies showed that EBAG9 also affects T lymphocyte activity in eliminating virus-infected cells.[11]

We previously demonstrated that the EBAG9 protein is secreted by extracellular vesicles in prostate cancer cells and affects the tumor microenvironment in a paracrine manner.[13] Moreover, the extracellular vesicles containing EBAG9 not only induce the endothelial-mesenchymal transition (EMT) of adjacent prostate cancer cells but also suppress the activity of T lymphocytes attacking prostate cancer cells. We identified TM9SF1 as an EBAG9 interacting molecule using yeast two-hybrid screening and demonstrated the physical interaction between the two proteins in HeLa cells. Functionally, TM9SF1 promotes EMT in prostate cancer cells. TM9SF1 was initially identified as a protein that induces autophagy[14]; however, the relationship between autophagy and the role of TM9SF1 in prostate cancer cells is yet to be clarified.

As described above, the pathological roles of EBAG9 in tumor biology and viral infections have been investigated in many studies. However, studies on the physiological functions of EBAG9 are limited. The bone tissue is known as an estrogen-affecting tissue where the beneficial effect of estrogen replacement therapy has been proven in a clinical trial.[15] Since we discovered *Ebag9* as an estrogen-induced gene, we hypothesized that some of the effects of estrogen on the bone tissue might be mediated by EBAG9. We also hypothesized that EBAG9 could regulate autophagy in the bone tissue, which was inspired by our previous study showing that EBAG9 interacts with the autophagy-promoting

[1]Department of Systems Aging Science and Medicine, Tokyo Metropolitan Institute for Geriatrics and Gerontology, Itabashi-ku, Tokyo 173-0015, Japan
[2]Department of Geriatric Medicine, Graduate School of Medicine, The University of Tokyo, Bunkyo-ku, Tokyo 113-8655, Japan
[3]Division of Systems Medicine and Gene Therapy, Saitama Medical University, Hidaka, Saitama 350-1241, Japan
[4]Department of Developmental Biology of Hard Tissue, Graduate School of Dental Medicine, Hokkaido University, Sapporo, Hokkaido 060-8586, Japan
[5]Department of Orthopedic Surgery, Saitama Medical University, Moroyama, Saitama 350-0495, Japan
[6]Department of Orthopedic Surgery, Japan Community Health Care Organization Saitama Northern Medical Center, Saitama, Saitama 331-8625, Japan
[7]Lead contact
*Correspondence: sinoue@tmig.or.jp
https://doi.org/10.1016/j.isci.2024.108871

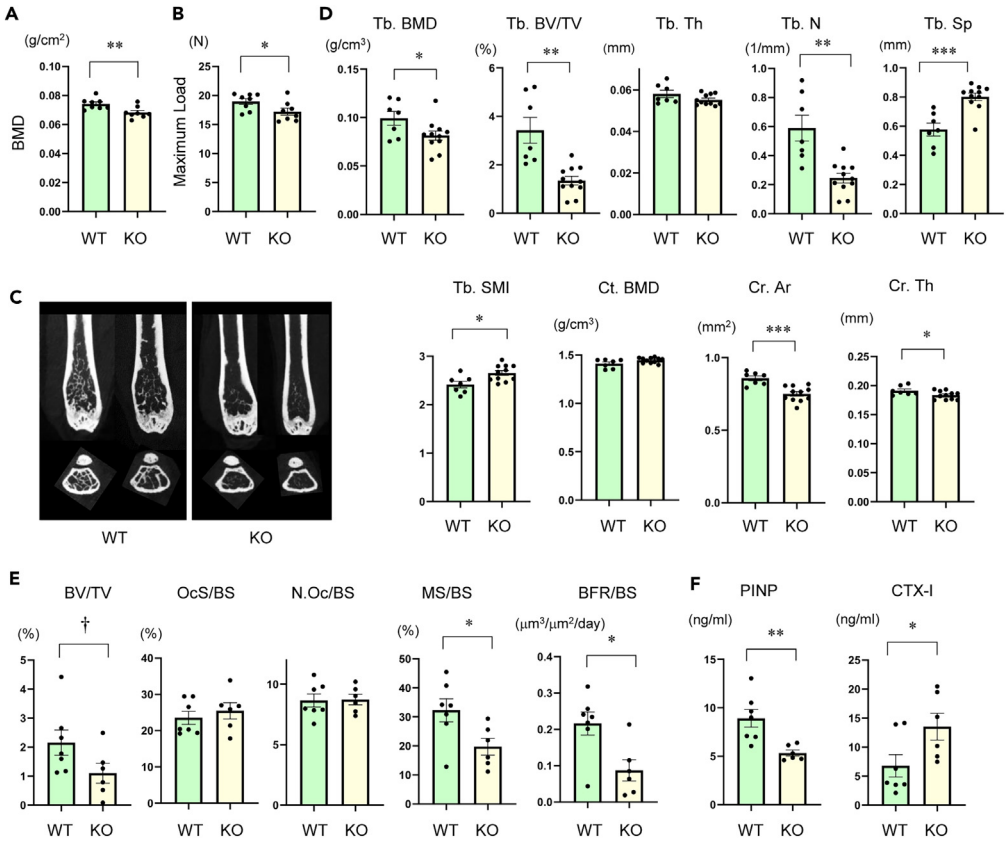

Figure 1. *Ebag9*-knockout mice display decreased bone mineral density with decreased bone formation

(A) Bone mineral densities (BMD) of femurs of 8-month-old female wild-type mice (WT; n = 8) and *Ebag9*-knockout mice (KO; n = 8) were evaluated using dual-energy X-ray absorptiometry (DXA). Results are expressed as mean ± SEM. **p < 0.01 (*t*-test).

(B) Maximum load calculated by three-point bending test using femoral diaphysis of 8-month-old female wild-type mice (WT; n = 8) and *Ebag9*-knockout mice (n = 8). Results are expressed as mean ± SEM. *p < 0.05 (*t*-test).

(C) Representative micro-CT images of distal femoral bones of 8-month-old female wild-type mice (WT) and *Ebag9*-knockout mice (KO).

(D) Microstructural parameters (Tb. BMD, bone mineral density of trabecular bone; Tb. BV/TV, bone volume fraction per tissue volume of trabecular bone; Tb.Th, trabecular thickness; Tb.N, trabecular number; Tb.Sp, trabecular separation; Tb.SMI, structure model index of trabecular bone; Ct. BMD, bone mineral density of cortical bone; Ct. Ar, cortical area; Ct. Th, cortical thickness) of distal femoral bones of 8-month-old female wild-type (WT; n = 7) and *Ebag9*-knockout mice (KO; n = 11) derived from micro-CT analysis are shown. Results are expressed as mean ± SEM. *p < 0.05, **p < 0.01, ***p < 0.001 (*t*-test).

(E) Histomorphometric parameters (BV/TV, bone volume to tissue volume; Oc.S/BS, osteoclast surface to bone surface; N.Oc/BS, osteoclast number to bone surface; MS/BS, mineralizing surface to bone surface; BFR/BS, bone formation rate to bone surface) of proximal tibial metaphysis from 9-month-old female wild-type mice (WT; n = 7) and *Ebag9*-knockout mice (KO; n = 6) are shown. Results are expressed as mean ± SEM. †p < 0.1, *p < 0.05 (*t*-test).

(F) Serum concentrations of procollagen I N-terminal propeptide (PINP) and cross-linked C-terminal telopeptide of type I collagen (CTX-I) of 9-month-old female wild-type mice (WT; n = 7) and *Ebag9*-knockout mice (KO; n = 6) are shown. Results are expressed as mean ± SEM. *p < 0.05, **p < 0.01 (*t*-test).

molecule TM9SF1. Autophagy is also involved in the bone metabolism. In animal experiments, both bone formation[16–18] and resorption[19,20] are affected by autophagy. In humans, it has been shown that autophagy-related genes are associated with wrist bone mineral density (BMD) by genome-wide association analysis.[21] Considering these backgrounds, we investigated the physiological functions of EBAG9 by focusing on the bone tissue by analyzing bone phenotypes in *Ebag9*-knockout mice.

RESULTS

EBAG9 has a bone-protective effect

To investigate the physiological functions of EBAG9, we focused on the bone phenotypes in *Ebag9*-knockout mice. First, the BMD of entire femoral bones from 8-month-old female *Ebag9*-knockout and wild-type mice was evaluated by dual-energy X-ray absorptiometry (DXA). BMD of bones from *Ebag9*-knockout mice was significantly lower than that of bones derived from wild-type mice (Figure 1A). The mechanical strength of femoral bones from 8-month-old female *Ebag9*-knockout and wild-type mice was evaluated using a three-point bending test. A significantly weaker force was required to cause fracture at the midpoint of the femoral bones from *Ebag9*-knockout mice than that required

to cause fracture to the bones of wild-type mice (Figure 1B). These results suggest that one of the physiological functions of EBAG9 is its bone-protective effect.

Next, the microstructure of the femoral bones from 9-month-old female *Ebag9*-knockout mice was evaluated using quantitative micro-computed tomography (micro-CT). Micro-CT images of the distal part of the femoral bones revealed decreased trabeculae and cortical thickness of the bones from *Ebag9*-knockout mice compared to those from wild-type mice (Figure 1C). The differences in gross appearance were substantiated by the parameters of both the trabecular and cortical bones in the distal part of the femoral bones (Figure 1D). The microstructure of femoral bones from 3-month-old female *Ebag9*-knockout mice, showed no significant difference between bones from wild-type mice and *Ebag9*-knockout mice (Figure S1), suggesting that the decreased bone mass of *Ebag9*-knockout mice is an age-dependent phenomenon. We also analyzed the microstructure of femoral bones from 10-month-old male *Ebag9*-knockout mice. No significant difference was observed between bones from wild-type and *Ebag9*-knockout mice (Figure S2), suggesting that sexual dimorphism exists in the bone phenotype of *Ebag9*-knockout mice.

Since *Ebag9* was originally identified as an estrogen-induced gene in breast cancer cells,[1] we hypothesized that EBAG9 expression in the bone tissue may be dependent on circulating estradiol. However, when we analyzed the effect of ovariectomy on the microstructure of femoral bones from *Ebag9*-knockout mice, a decrease in bone mineral density and bone volume was observed in both wild-type and *Ebag9*-knockout mice, with a more prominent effect observed in *Ebag9*-knockout mice (Figure S3). The difference in bone phenotype between ovariectomized *Ebag9*-knockout mice and ovariectomized wild-type mice suggests that EBAG9 is also expressed in ovariectomized mice and that estrogen may not be a determinant factor of EBAG9 expression in the bone tissue.

Decreased bone formation in *Ebag9*-knockout mice

To investigate the mechanisms underlying decreased bone mass and microstructural changes in the bones of *Ebag9*-knockout mice, histomorphometric analysis with calcein double staining was performed on 9-month-old female mice. Bone histomorphometric analysis of the proximal tibia revealed that the mineralizing surface-to-bone surface (MS/BS) and bone formation rate to bone surface (BFR/BS) were significantly decreased in the bones of *Ebag9*-knockout mice, whereas parameters related to osteoclasts were not significantly different (Figure 1E). This result suggests that the bone-protective effect of EBAG9 is mainly caused by enhanced bone formation. Bone turnover markers were evaluated using serum obtained from 9-month-old female mice at the time of euthanasia. The serum concentration of procollagen I N-terminal peptide (PINP), which reflects bone formation, was significantly lower in the serum obtained from *Ebag9*-knockout mice compared to that of wild-type mice (Figure 1F). This result aligns with the histomorphometric data showing reduced bone formation in *Ebag9*-knockout mice. Furthermore, the serum concentration of the cross-linked C-terminal telopeptide of type I collagen (CTX-I), which reflects bone resorption, was significantly elevated in the serum obtained from *Ebag9*-knockout mice compared to that of wild-type mice (Figure 1F). This result suggests that the suppression of bone resorptive activity may also contribute to the bone protective effect of EBAG9. Immunohistochemical analysis of the femoral trabecular bone using the EBAG9 antibody revealed cytoplasmic staining in both osteoblasts and osteoclasts (Figure S4), suggesting that EBAG9 has biological roles in both osteoblastic and osteoclastic lineages.

EBAG9 is required for normal differentiation of osteoblastic cells

Based on the results of the histomorphometric analysis, we concluded that EBAG9 primarily functions in the osteoblastic lineage. Therefore, we investigated the effects of EBAG9 on osteoblastic differentiation. Primary osteoblasts were isolated from the calvariae of female *Ebag9*-knockout and wild-type mice. The cells were then cultured in a differentiation-inducing medium. Alkaline phosphatase activity evaluated at 2 weeks of differentiation was weaker in primary osteoblasts derived from three individual *Ebag9*-knockout mice than those derived from three individual wild-type mice (Figure 2A). Mineralization of primary osteoblasts was evaluated by prolonged culture for 5 weeks in a differentiation-inducing medium. Impaired calcification was observed in primary osteoblasts derived from *Ebag9*-knockout mice compared to primary osteoblasts derived from wild-type mice (Figures 2B and 2C). Impaired differentiation of primary osteoblasts derived from *Ebag9*-knockout mice was also shown by the suppressed induction of the alkaline phosphatase (*Alp*) gene by the differentiation-inducing medium (Figure 2D). Impaired differentiation of EBAG9-deficient osteoblasts was also observed when we used primary osteoblasts derived from male *Ebag9*-knockout and wild-type mice (Figure S5A). We evaluated the effect of Ebag9 knockdown on osteoblastic differentiation of the preosteoblastic cell line MC3T3-E1. We designed siRNAs specific to murine *Ebag9* and confirmed the existence of *Ebag9* mRNA in MC3T3-E1 cells and the effects of siRNAs targeting *Ebag9* (Figure 2E). We then evaluated the expression of *Alp* in MC3T3-E1 cells when they were cultured in a differentiation-inducing medium after *Ebag9* knockdown. Induction of *Alp* by the differentiation-inducing medium was suppressed in MC3T3-E1 cells treated with siRNAs (Figure 2F). These results indicated that one of the physiological functions of EBAG9 in the osteoblastic lineage is to maintain normal differentiation.

EBAG9 has an autophagy-promoting effect in osteoblastic lineage

We previously discovered TM9SF1 as an EBAG9 interacting molecule in HeLa cells.[13] Since TM9SF1 is reported to have an autophagy-promoting effect,[14] we hypothesized that EBAG9 has some effects on autophagy. To investigate the possibility that EBAG9 is related to autophagy, we utilized EGFP-LC3B, a fusion protein of LC3B and enhanced green fluorescent protein (EGFP), and EBAG9-DsRed, a fusion protein of EBAG9 and DsRed. Co-transfection of plasmids encoding EGFP-LC3B and EBAG9-DsRed in MC3T3-E1 cells revealed the co-localization of LC3B and EBAG9 (Figure 3A). This result suggests that EBAG9 functions in autophagosomes in preosteoblastic cells. Since the localization of EBAG9 in the Golgi apparatus has been reported in tumor cells,[3] we evaluated whether EBAG9 was also localized to the Golgi apparatus in

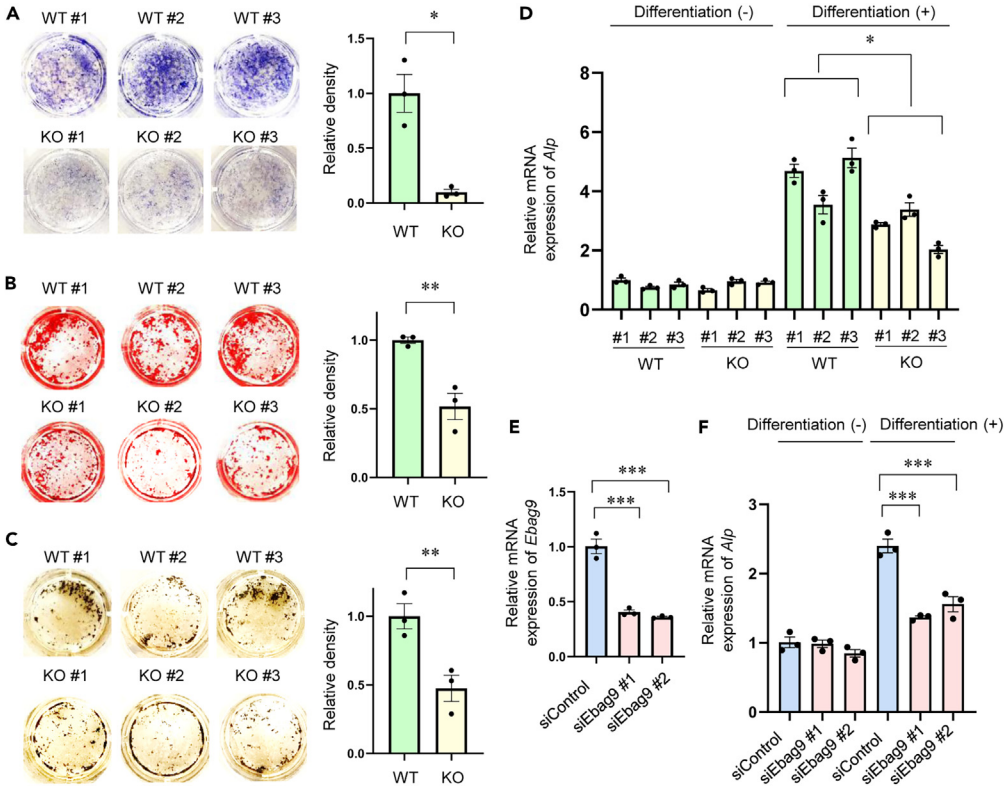

Figure 2. EBAG9-deficient osteoblasts display suppressive differentiation

(A) Alkaline phosphatase activity in primary osteoblasts derived from female wild-type mice (WT; n = 3) and *Ebag9*-knockout mice (n = 3). The activities were analyzed after culturing primary osteoblasts with a differentiation-inducing medium containing β-glycerophosphate (10 mM) and L-ascorbic acid 2-phosphate (0.2 mM) for 2 weeks. Quantified stained area was shown in the bar graph as mean ± SEM (n = 3). Relative values were shown with a mean stained area of the wild-type cells as the reference value. *p < 0.05 (*t*-test).

(B and C) Alizarin Red staining (B) and von Kossa staining (C) of primary osteoblasts derived from female wild-type mice (WT; n = 3) and *Ebag9*-knockout mice (n = 3) after culturing primary osteoblasts with differentiation medium for 5 weeks. Quantified stained area was shown in the bar graph as mean ± SEM (n = 3). Relative values were shown with a mean stained area of the wild-type cells as the reference value. **p < 0.01 (*t*-test).

(D) Expression of alkaline phosphatase *(Alp)* in primary osteoblasts derived from female wild-type mice (WT; n = 3) and *Ebag9*-knockout mice (n = 3). The cells were analyzed with qRT-PCR after they were cultured with a differentiation-inducing medium or α-MEM not containing β-glycerophosphate or L-ascorbic acid 2-phosphate for 7 days. The relative RNA levels were determined by normalization with *Gapdh* expression. Results are shown as mean fold change over WT#1 without differentiation-inducing medium ±SEM (n = 3). *p < 0.05 (two-way ANOVA).

(E and F) Knockdown of *Ebag9* expression with si*Ebag9* in MC3T3-E1 cells was performed by reverse transfection method. Two kinds of siRNAs for *Ebag9* (siEbag9 #1 and #2) and an siRNA not targeting human transcripts (siControl) were used. Cells were cultured with a differentiation-inducing medium or α-MEM not containing β-glycerophosphate or L-ascorbic acid 2-phosphate for 2 days (E) or 7 days (F) after siRNA transfection. Total RNA was extracted and the expression levels of *Ebag9* or alkaline phosphatase *(Alp)* were analyzed with qRT-PCR. The relative RNA levels were determined by normalization with *Gapdh* expression. Results are shown as mean fold change over siControl without differentiation-inducing medium ±SEM (n = 3). ***p < 0.001 (Dunnett's test).

MC3T3-E1 cells. EBAG9 showed the partial co-localization with a Golgi-resident enzyme (Figure S6). These results indicate that EBAG9 can localize to the autophagosome and the Golgi apparatus.

Next, we evaluated the effect of EBAG9 on the amounts of p62 protein, also known as sequestosome 1 (SQSTMI), and lipidation of LC3B in MC3T3-E1 cells. Conversion of LC3-I to LC3-II and degradation of p62 reflect the autophagic activity of the cell.[22,23] The lipidated form (LC3-II) migrates faster than the non-lipidated form (LC3-I) in SDS-PAGE, although LC3-II has a higher molecular weight than LC3-I.[24] When MC3T3-E1 cells were transfected with a plasmid encoding EBAG9, lower amounts of p62 protein and LC3-I were observed in EBAG9 overexpressing cells (Figure 3B). When *Ebag9* was knocked down, higher amounts of p62 protein and non-lipidated form of LC3B (LC3-I) were observed (Figure 3C). We then evaluated the amounts of p62 protein and lipidation of LC3B in primary osteoblasts. In primary osteoblasts derived from female *Ebag9*-knockout mice, higher amounts of p62 protein and the non-lipidated form of LC3B (LC3-I) were observed than in osteoblasts derived from wild-type mice (Figure 3D). These results suggest that EBAG9 promotes autophagy in the osteoblastic lineage. Impaired autophagy was observed in primary osteoblasts derived from male *Ebag9*-knockout mice (Figure S5B).

Ultrastructural analysis of femoral bones from a 5-month-old female wild-type mouse and an *Ebag9*-knockout mouse revealed that osteocytes in a *Ebag9*-knockout mouse tended to contain a relatively wider cytosolic area with more subcellular organelles than osteocytes in a

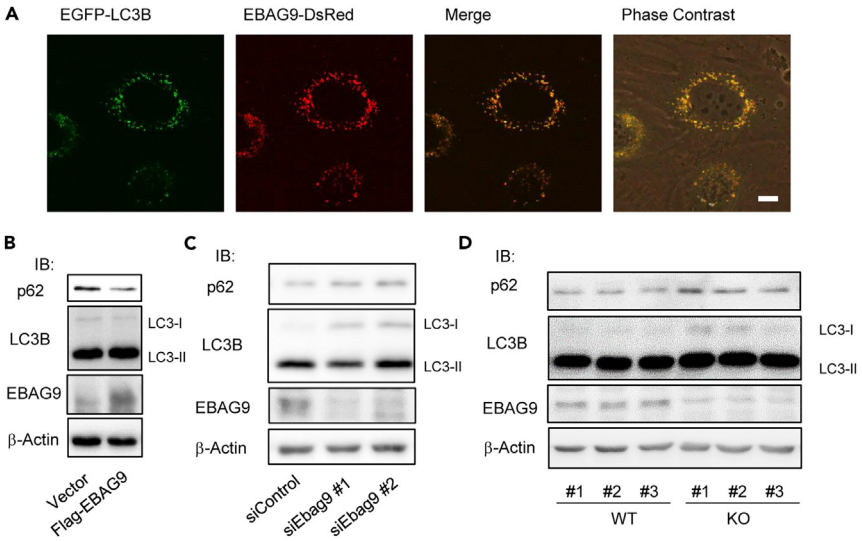

Figure 3. EBAG9 promotes autophagy in osteoblastic lineage

(A) Fluorescence microscopy images of MC3T3-E1 cells co-expressing EGFP-LC3B (green color) and EBAG9-DsRed (red color). Scale bar; 10 μm.

(B) Forty-eight hours after transfection with a plasmid encoding Flag-EBAG9 or an empty vector, MC3T3-E1 cells were treated with pepstatin A (10 μg/mL) and E64d (10 μg/mL) for 5 h before cell lysis. Western blotting was performed to detect p62, LC3B, and EBAG9. β-actin protein was blotted as an internal control. IB; immunoblot.

(C) Forty-eight hours after transfection of indicated siRNAs (10 nM), MC3T3-E1 cells were treated with pepstatin A (10 μg/mL) and E64d (10 μg/mL) for 5 h before cell lysis. Western blotting was performed to detect p62, LC3B, and EBAG9. β-actin protein was blotted as an internal control. IB; immunoblot.

(D) Primary osteoblasts derived from female wild-type mice (WT; n = 3) and *Ebag9* knockout mice (n = 3) were treated with pepstatin A (10 μg/mL) and E64d (10 μg/mL) for 5 h before cell lysis. Western blotting was performed to detect p62, LC3B, and EBAG9. β-actin protein was blotted as an internal control. IB; immunoblot.

wild-type mouse, resulting in a significantly lower nuclear-to-cytoplasm ratio in EBAG9-deficient osteocytes (Figures 4A–4C and S7). Considering that autophagy is responsible for the degradation of subcellular organelles in osteocytes, this finding indirectly supports autophagy suppression in *Ebag9*-knockout mice.

EBAG9-deficient osteoclasts display enhanced differentiation and pit-forming activity

Since the serum concentration of CTX-I was significantly elevated in the serum obtained from *Ebag9*-knockout mice compared to that in the serum from wild-type mice (Figure 1F), we assumed the minor effect of EBAG9 on osteoclastic function, although deletion of EBAG9 did not affect parameters related to bone resorption in the histomorphometric analysis (Figure 1E). First, we evaluated the osteoclastic differentiation of bone marrow cells derived from *Ebag9*-knockout mice. TRAP staining after culturing in a differentiation-inducing medium revealed a tendency of enhanced differentiation of EBAG9-deficient bone marrow cells compared with bone marrow cells derived from wild-type mice, although this effect was not statistically significant (Figure S8A). Next, the effect of EBAG9 on osteoclastic differentiation was evaluated using the murine macrophage cell line RAW264.7. A significantly larger number of TRAP-positive cells were observed when RAW264.7 cells were differentiated after treatment with siRNAs targeting *Ebag9* compared with when they were treated with a control siRNA (Figure S8B). Enhanced osteoclastic differentiation of *Ebag9* knocked-down RAW264.7 cells was supported by increased expression of the *Ctsk* gene, a gene characteristic of differentiated osteoclasts, compared with RAW264.7 cells treated with a control siRNA when they were cultured in a differentiation-inducing medium (Figure S8C). Finally, the bone resorption activity of the differentiated RAW264.7 was estimated using culture plates coated with calcium phosphate. A significantly larger pit area was observed in the wells in which RAW264.7 cells were treated with siRNAs targeting *Ebag9* than in the wells in which RAW264.7 cells were treated with a control siRNA (Figure S8D), suggesting that the effect of EBAG9 on osteoclastic differentiation reflected bone resorptive activity.

EBAG9 has an autophagy-promoting effect in osteoclastic lineage

Next, we investigated whether EBAG9 affected autophagy in the osteoclastic lineage. Co-transfection of plasmids encoding EGFP-LC3B and EBAG9-DsRed in RAW264.7 revealed partial co-localization of LC3B and EBAG9 (Figure S9A). This result suggests that EBAG9 functions in autophagosomes in RAW264.7 cells. EBAG9 was also localized to the Golgi apparatus in RAW264.7 cells (Figure S9B), indicating that EBAG9 can localize to both autophagosomes and the Golgi apparatus. Next, we evaluated the effect of EBAG9 overexpression on the amounts of p62 protein and lipidation of LC3B in RAW264.7 cells. When EBAG9 was overexpressed in RAW264.7 by infecting adenovirus vector encoding EBAG9, lower amounts of p62 protein and higher amounts of lipidated form of LC3B (LC3-II) were detected compared with RAW264.7 cells

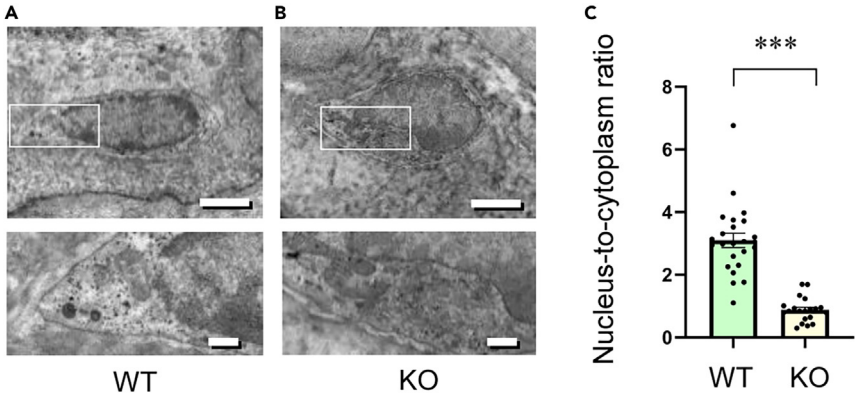

Figure 4. Osteocytes in *Ebag9*-knockout mice display a lower nucleus-to-cytoplasm ratio and contain more subcellular organelle

(A and B) Representative transmission electron micrographs of femoral bones from a 5-month-old wild-type mouse (WT) and an *Ebag9*-knockout mouse (KO). Indicated areas in the upper panels are enlarged in the lower panels. Scale bars: 2 μm (upper panels), 500 nm (lower panels).

(C) Nucleus-to-cytoplasm ratios of osteocytes were analyzed based on the transmission electron micrographs derived from 24 cells from a wild-type mouse and 20 cells from a knockout mouse including cells shown in Figures 4A, 4B, and S7. Results are expressed as mean ± SEM. ***$p < 0.001$ (*t*-test).

infected with control adenovirus vector (Figure S9C). When RAW264.7 cells were transfected with siRNAs targeting *Ebag9*, higher amounts of p62 protein and lower amounts of LC3-II were detected in *Ebag9* knockdown cells than in cells transfected with a control siRNA (Figure S9D). These results suggest that EBAG9 promotes autophagy in the osteoclastic lineage. We then evaluated the amounts of p62 protein and lipidation of LC3B in primary osteoclast precursor cells. In primary osteoclast precursor cells derived from male and female *Ebag9*-knockout mice, higher amounts of p62 protein were observed compared with osteoclast precursor cells derived from wild-type mice (Figures S9E and S9F). LC3-I was undetectable under the experimental conditions. These results suggest that EBAG9 promotes autophagy in the osteoblastic lineage.

TM9SF1-deficient preosteoblastic cells display suppressed differentiation and reduced autophagy

Finally, we explored the role of the EBAG9 interacting molecule TM9SF1 in the osteoblastic lineage. The role of TM9SF1 in promoting autophagy was originally demonstrated by the experiments using HeLa cells.[13] Therefore, we assumed the autophagy-promoting effect of TM9SF1 in osteoblastic cells. Immunohistochemical analysis of the femoral trabecular bone using the TM9SF1 antibody revealed cytoplasmic staining in both osteoblasts and osteoclasts (Figure S10). We designed siRNAs specific to murine *Tm9sf1* and confirmed the presence of *Tm9sf1* mRNA in MC3T3-E1 cells as well as the effects of siRNAs targeting *Tm9sf1* (Figure 5A). We then evaluated autophagy marker proteins in MC3T3-E1 cells when *Tm9sf1* was knocked down. MC3T3-E1 cells transfected with siRNAs targeting *Ebag9* displayed higher amounts of p62 protein and higher amounts of LC3-I (Figure 5B), indicating that autophagy was suppressed in *Tm9sf1* knocked-down MC3T3-E1 cells. To investigate the effect of TM9SF1 on osteoblastic differentiation, MC3T3-E1 cells treated with siRNAs targeting *Tm9sf1* were cultured in a differentiation-inducing medium. Alkaline phosphatase activity evaluated on day 11 of differentiation was weaker in the cells treated with siRNAs targeting *Tm9sf1* than in cells treated with a control siRNA (Figure 5C). Impaired differentiation of MC3T3-E1 cells treated with siRNAs targeting *Tm9sf1* was also shown by the suppressed induction of *Alp* expression in a differentiation-inducing medium (Figure 5D). Finally, we overexpressed TM9SF1 in the *Ebag9* knockdown cells and evaluated the expression of autophagy marker proteins. The elevated levels of p62 and LC3-I in *Ebag9* knockdown cells were decreased by TM9SF1 overexpression in MC3T3-E1 cells (Figure 5E), suggesting that TM9SF1 promotes autophagy in the osteoblastic lineage and contributes to osteoblastic differentiation, together with EBAG9. Figure 5F shows a schematic representation of the role of EBAG9 in the bone tissue.

DISCUSSION

In the present study, we demonstrated that EBAG9 plays a key physiological role in maintaining the murine skeleton. Our findings indicate the role of EBAG9 in the bone tissue, in addition to its known role in tumor cells, particularly in the context of immune escape. Analyses of the bone phenotype of *Ebag9*-knockout mice revealed that the mice had fragile bones with lower bone mineral density than wild-type mice. Micro-CT analyses revealed that genetic deletion of *Ebag9* affected both trabecular and cortical bones. The results of histomorphometric analyses indicated that the genetic deletion of *Ebag9* predominantly affected bone formation parameters. Serum bone turnover markers showed that enhanced bone resorption also contributed to this phenotype. We also demonstrated the suppressed osteoblastic differentiation of EBAG9-deficient preosteoblastic cells. These observations suggest that EBAG9 has a bone-protective effect, predominantly by supporting normal bone formation (Figure 5F).

To the best of our knowledge, this is the first study to report the functional relationship between EBAG9 and autophagy. Autophagy has been suggested to be associated with human bone metabolism. According to the results of pathway-based genome-wide association

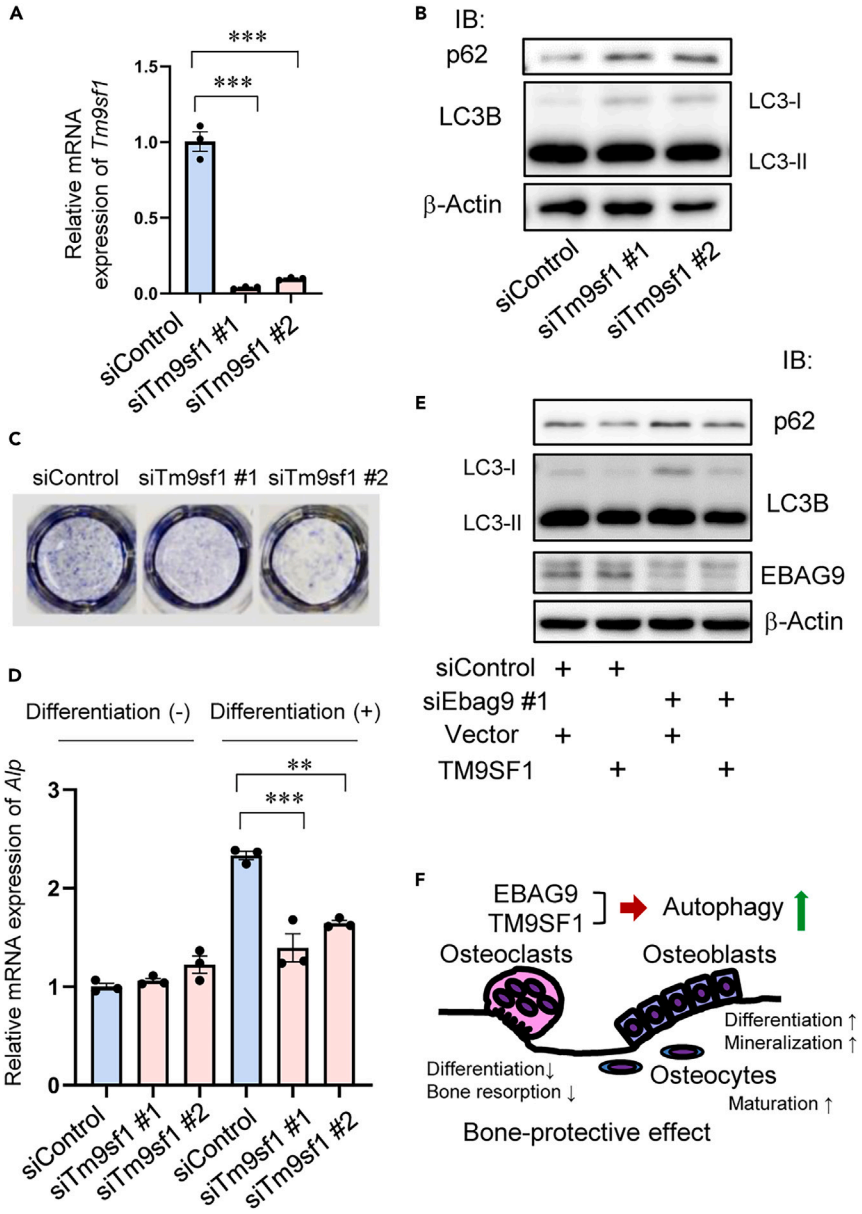

Figure 5. TM9SF1-deficient preosteoblastic cells display suppressed differentiation and reduced autophagy

(A) Knockdown of *Tm9sf1* expression with siTm9sf1 in MC3T3-E1 cells was performed by reverse transfection method. Two kinds of siRNAs for *Tm9sf1* (siTm9sf1 #1 and #2) and an siRNA not targeting human transcripts (siControl) were used. Forty-eight h after transfection of indicated siRNAs (10 nM), total RNA was extracted. The expression levels of *Tm9sf1* were analyzed with qRT-PCR. The relative RNA levels were determined by normalization with *Gapdh* expression. Results are shown as mean fold change over siControl ±SEM (n = 3). ***p < 0.001 (Dunnett's test).

(B) Forty-eight h after transfection of indicated siRNAs (10 nM), MC3T3-E1 cells were treated with pepstatin A (10 μg/mL) and E64d (10 μg/mL) for 5 h before cell lysis. Western blotting was performed to detect p62 and LC3B. β-actin protein was blotted as an internal control. IB; immunoblot.

(C) Activities of alkaline phosphatase in MC3T3-E1 cells treated with indicated siRNAs (10 nM) by reverse transfection method. The activities were analyzed after culturing the cells with a differentiation-inducing medium containing β-glycerophosphate (10 mM) and L-ascorbic acid 2-phosphate (0.2 mM) for 11 days.

(D) MC3T3-E1 cells were cultured with a differentiation-inducing medium or α-MEM not containing β-glycerophosphate or L-ascorbic acid 2-phosphate for 7 days after transfection of indicated siRNAs (10 nM). Total RNA was extracted and the expression levels of alkaline phosphatase *(Alp)* were analyzed with qRT-PCR. The relative RNA levels were determined by normalization with *Gapdh* expression. Results are shown as mean fold change over siControl without differentiation-inducing medium ±SEM (n = 3). **p < 0.01, ***p < 0.001 (Dunnett's test).

(E) MC3T3-E1 cells transfected with indicated siRNAs (10 nM) were transfected with a plasmid encoding TM9SF1 or an empty vector on the next day of siRNA transfection. Forty-eight h after siRNA transfection, cells were lysed and subjected to western blot analysis. Indicated antibodies were used for blotting. IB; immunoblot.

(F) A schematic model of bone-protective effects of EBAG9 and its interacting protein TM9SF1.

analysis, the regulation of the autophagy pathway, including genes such as *ATG5, ATG7,* and *ATG12*, was most significantly associated with the BMD of the distal radius in the U.S. population.[21] The missense mutation of p62 was shown to be associated with Paget's disease of bone,[25] a disorder caused by abnormally increased and disorganized bone turnover. It was formerly shown that autophagy in osteoblastic lineage has a bone-protective effect. Reduced bone mass was observed in osteoblast-specific autophagy-deficient mice, in which ATG5 or ATG7, molecules involved in the autophagic process, were conditionally deleted in osteoblastic lineage using Cre recombinase under the control of *Col1a* (collagen, type I, α)-Cre promoter.[16,17] These studies also demonstrated the impaired differentiation and mineralization of primary osteoblasts derived from autophagy-deficient mice. Our results are in line with the differentiation-promoting function of autophagy in osteoblastic cells because we showed that EBAG9 promoted autophagy and that EBAG9-deficient osteoblasts displayed impaired differentiation and mineralization. It was also reported that autophagy in the osteoblastic lineage affects osteocyte maturation by analyzing osteoblast-specific *Atg7*-knockout mice using Cre recombinase under the control of *Osterix 1* promoter.[18] Loss of autophagy in osteoblasts resulted in impaired maturation of osteocytes with a significantly lower nucleus-to-cytoplasm ratio. Therefore, the lower nucleus-to-cytoplasm ratio in the osteocytes of *Ebag9*-knockout mice compared to wild-type mice in this study presumably indicates impaired maturation of osteocytes due to the suppression of autophagy.

As we previously showed that TM9SF1 functionally interacts with EBAG9,[13] we hypothesized that EBAG9 affects autophagy in the bone tissue by collaborating with TM9SF1. The contribution of TM9SF1 to autophagy was previously shown in HeLa cells.[14] In this study, we demonstrated that TM9SF1 has autophagy-promoting effects even in MC3T3-E1 osteoblastic cells with reduced autophagy due to EBAG9 silencing and that loss- and gain-of-function of TM9SF1 could modulate osteoblastic differentiation along with autophagy.

The relationship between autophagy and bone resorption in the osteoclastic lineage is complex. One reason for this is that molecules that are important in autophagy are also involved in bone resorption. For example, ATG5 plays an essential role in the formation of ruffled borders in osteoclasts. Therefore, suppressed autophagy coincides with decreased bone resorption in osteoclast-specific *Atg5*-knockout mice.[19] Moreover, p62 plays a distinct role in receptor activator of nuclear factor kappa-B ligand (RANKL)-induced osteoclastogenesis,[20] suggesting that autophagy-dependent degradation of p62 could inhibit osteoclastogenesis. Another reason for the complicated relationship between autophagy and bone resorption is that they sometimes share the same upstream signaling. For example, the mammalian target of rapamycin (mTOR) regulates osteoclastogenesis and autophagy. In this case, the inhibition of mTOR leads to increased autophagy, which coincides with decreased bone resorption,[26,27] resulting in an opposite relationship between autophagy and bone resorption compared to that in *Atg5*-knockout mice. In our study, we showed that the loss of EBAG9 had a minor effect on enhanced bone resorption in *Ebag9*-knockout mice, as evaluated by serum CTX-I. Although further studies are required, this result could be partly explained by the decreased degradation of p62 due to the possible activation of mTOR in the absence of EBAG9. Alternatively, it may be dependent on other pathways that simultaneously suppress autophagy and activate osteoclastic functions.

We observed enhanced differentiation and bone resorptive function in RAW 264.7 cells treated with siEBAG9 under the stimulation of sRANKL. Meanwhile, the results of our histomorphometric analyses indicated that genetic deletion of *Ebag9* did not significantly affect the parameters of bone resorption, whereas data on serum turnover markers showed enhanced bone resorption. Although the reason for this discrepancy between the results of histomorphometric analyses and the serum turnover marker is not clear, we speculate that the loss of EBAG9 function more profoundly affected on the bone-resorptive function of osteoclasts, reflected by the serum turnover marker, than on the differentiation of osteoclast precursors which was quantified by bone histomorphometry. It is also possible that the differentiation of osteoclast precursors was enhanced in bones other than the tibia in *Ebag9*-knockout mice. Another possibility is that endogenous osteoblast-derived RNAKL is not strong enough to induce differences in osteoclastic differentiation, as shown in an *in vitro* experiment using soluble RANKL.

It has been shown that autophagic activity in osteocytes declines age-dependently by analyzing proteins extracted from murine cortical bones.[28] In that study, the amounts of LC3-II was decreased in 24-month-old mice in both male and female mice in comparison with proteins extracted from cortical bones from 2-month-old and 24-month-old mice.[28] When the autophagic activities of primary osteoblasts isolated from the bone marrow of 2-month-old and 24-month-old mice were compared, a decreased autophagic activity was observed only in female mice,[28] indicating that sexual dimorphism may exist in the age-related decline of autophagic activity in osteoblasts. Intriguingly, ovariectomy did not alter the autophagic activity of the protein extracted from cortical bones,[28] suggesting that the aging-dependent decline in autophagic activity in female osteocytes is not mediated by the decreased production of estrogen from the ovaries. We also observed sexual dimorphism in the analysis of bone phenotypes in *Ebag9*-knockout and wild-type mice, in which a significant pathological phenotype was observed only in female *Ebag9*-knockout mice. We first hypothesized that estrogen could be involved in the sexual dimorphism of EBAG9 function, since *Ebag9* was originally identified as an estrogen-induced gene in breast cancer cells. However, the contribution of estrogen to the EBAG9-dependent bone phenotype may be minimal because deletion of EBAG9 affects the bone phenotype, even in ovariectomized mice. Since primary cultured osteoblasts and primary cultured bone marrow macrophages derived from *Ebag9*-knockout mice displayed reduced autophagic activity compared with those derived from wild-type mice, sexual dimorphism may exist only *in vivo*. We speculated that the hormonal environment in male mice might affect the expression or function of EBAG9 and/or TM9SF1.

Our results provide information on potential therapeutic options for age-dependent osteoporosis in females by identifying or developing molecules or chemicals that upregulate the expression of EBAG9 and/or TM9SF1 in the bone. Autophagy-activating drugs, such as rapamycin and metformin, are reported to have bone-protective effects in mice and rats,[29,30] implying that a strategy targeting autophagy might be feasible for the prevention and/or treatment of osteoporosis in the near future.

In conclusion, we demonstrated the bone-protective role of EBAG9, which could be one of its physiological functions of EBAG9. The bone-protective role is accompanied by the promotion of autophagy, as EBAG9-deficient cells display suppressive autophagy. Based on our finding that EBAG9 interacts with TM9SF1, which has been reported to have an autophagy-promoting effect, we propose that EBAG9 exerts an autophagy-promoting effect together with its interactor, TM9SF1.

Limitation of the study

The possibility that the phenotype of *Ebag9*-knockout mice is derived from functions of EBAG9 and TM9SF1 other than autophagic regulation was not excluded from our study. In addition, the mechanism underlying the sexually dimorphic phenotype of *Ebag9*-knockout mice was not elucidated in the present study. Future studies on autophagic regulation or EBAG9 function in human bones are required, as all the data presented in this study were derived from murine models or cells derived from mice.

STAR★METHODS

Detailed methods are provided in the online version of this paper and include the following:

- KEY RESOURCES TABLE
- RESOURCE AVAILABILITY
  - Lead contact
  - Materials availability
  - Date and code availability
- EXPERIMENTAL MODEL AND STUDY PARTICIPANT DETAILS
  - Generation of *Ebag9*-knockout mice
  - Animal experiments
  - Isolation of primary osteoblasts
  - Isolation of primary osteoclast precursors
  - Cell culture
  - Osteogenic differentiation
  - Osteoclastic differentiation
- METHOD DETAILS
  - Bone mineral density (BMD) measurements
  - Three-point bending test
  - Quantitative micro-computed tomography
  - Bone histomorphometry
  - Bone immunohistochemistry
  - Transmission electron microscopic (TEM) analysis
  - Enzyme-linked immunosorbent assay (ELISA)
  - Antibodies and reagents
  - Evaluation of alkaline phosphatase activity
  - Alizarin red staining
  - Von Kossa staining
  - TRAP staining
  - Pit formation assay
  - Quantitative reverse transcription polymerase chain reaction
  - Plasmid construction and transfection
  - Fluorescence microscopy imaging
  - Small interfering RNA transfection
  - Western blot analysis
- QUANTIFICATION AND STATISTICAL ANALYSIS

SUPPLEMENTAL INFORMATION

Supplemental information can be found online at https://doi.org/10.1016/j.isci.2024.108871.

ACKNOWLEDGMENTS

We thank Dr. T. Takeiwa and Ms. N. Sasaki for their assistance. This study was supported by grants from the Cell Innovation Program (S.I.), P-DIRECT (S.I.) and P-CREATE (S.I.) from the Ministry of Education, Culture, Sports, Science and Technology (MEXT), Japan; by Grants-in-Aid for S.I. (Grant nos. 15K15353, 20K21667, and 21H04829) and for K.A. (Grant nos. 17K10571 and 20K08945) from the Japan Society for the Promotion of Science (JSPS), Japan; by a grant from Uehara Memorial Foundation (S.I.); and by a grant from Japan Osteoporosis Foundation (K. A.).

AUTHOR CONTRIBUTIONS

Conceptualization, K.A., K.I., S.S., and S.I.; Investigation, K.A., K.I., S.S., W.S., T.H., N.A., and S.T.; Formal Analysis, K.A., K.I., S.S., and K.H.; Writing–Original Draft, K.A.; Writing–Review and Editing, all authors; Funding Acquisition, K.A. and S.I.

DECLARATION OF INTERESTS

The authors declare no competing interests.

Received: March 25, 2023
Revised: November 22, 2023
Accepted: January 8, 2024
Published: January 11, 2024

REFERENCES

1. Watanabe, T., Inoue, S., Hiroi, H., Orimo, A., Kawashima, H., and Muramatsu, M. (1998). Isolation of estrogen-responsive genes with a CpG island library. Mol. Cell Biol. *18*, 442–449.
2. Nakashima, M., Sonoda, K., and Watanabe, T. (1999). T. Inhibition of cell growth and induction of apoptotic cell death by the human tumor-associated antigen RCAS1. Nat. Med. *5*, 938–942.
3. Engelsberg, A., Hermosilla, R., Karsten, U., Schülein, R., Dörken, B., and Rehm, A. (2003). The Golgi protein RCAS1 controls cell surface expression of tumor-associated O-linked glycan antigens. J. Biol. Chem. *278*, 22998–23007.
4. Rüder, C., Reimer, T., Delgado-Martinez, I., Hermosilla, R., Engelsberg, A., Nehring, R., Dörken, B., and Rehm, A. (2005). EBAG9 adds a new layer of control on large dense-core vesicle exocytosis via interaction with Snapin. Mol. Biol. Cell *16*, 1245–1257.
5. Wolf, J., Reimer, T.A., Schuck, S., Rüder, C., Gerlach, K., Müller, E.C., Otto, A., Dörken, B., and Rehm, A. (2010). Role of EBAG9 protein in coat protein complex I-dependent glycoprotein maturation and secretion processes in tumor cells. Faseb. J. *24*, 4000–4019.
6. Takahashi, S., Urano, T., Tsuchiya, F., Fujimura, T., Kitamura, T., Ouchi, Y., Muramatsu, M., and Inoue, S. (2003). EBAG9/RCAS1 expression and its prognostic significance in prostatic cancer. Int. J. Cancer *106*, 310–315.
7. Ogushi, T., Takahashi, S., Takeuchi, T., Urano, T., Horie-Inoue, K., Kumagai, J., Kitamura, T., Ouchi, Y., Muramatsu, M., and Inoue, S. (2005). Estrogen receptor-binding fragment-associated antigen 9 is a tumor-promoting and prognostic factor for renal cell carcinoma. Cancer Res. *65*, 3700–3706.
8. Kumagai, J., Urano, T., Ogushi, T., Takahashi, S., Horie-Inoue, K., Fujimura, T., Azuma, K., Muramatsu, M., Ouchi, Y., Kitamura, T., and Inoue, S. (2009). EBAG9 is a tumor-promoting and prognostic factor for bladder cancer. Int. J. Cancer *124*, 799–805.
9. Fujimura, T., Takahashi, S., Urano, T., Xiaoqiang, L., Ogushi, T., Muramatsu, M., Ouchi, Y., Kitamura, T., Homma, Y., and Inoue, S. (2009). Estrogen receptor-binding fragment-associated gene 9 expression and its clinical significance in human testicular cancer. Int. J. Urol. *16*, 329–332.
10. Ijichi, N., Shigekawa, T., Ikeda, K., Miyazaki, T., Horie-Inoue, K., Shimizu, C., Saji, S., Aogi, K., Tsuda, H., Osaki, A., et al. (2013). Association of positive EBAG9 immunoreactivity with unfavorable prognosis in breast cancer patients treated with tamoxifen. Clin. Breast Cancer *13*, 465–470.
11. Rüder, C., Höpken, U.E., Wolf, J., Mittrücker, H.W., Engels, B., Erdmann, B., Wollenzin, S., Uckert, W., Dörken, B., and Rehm, A. (2009). The tumor-associated antigen EBAG9 negatively regulates the cytolytic capacity of mouse CD8+ T cells. J. Clin. Invest. *119*, 2184–2203.
12. Miyazaki, T., Ikeda, K., Horie-Inoue, K., Kondo, T., Takahashi, S., and Inoue, S. (2014). EBAG9 modulates host immune defense against tumor formation and metastasis by regulating cytotoxic activity of T lymphocytes. Oncogenesis *3*, e126.
13. Miyazaki, T., Ikeda, K., Sato, W., Horie-Inoue, K., and Inoue, S. (2018). Extracellular vesicle-mediated EBAG9 transfer from cancer cells to tumor microenvironment promotes immune escape and tumor progression. Oncogenesis *7*, 7.
14. He, P., Peng, Z., Luo, Y., Wang, L., Yu, P., Deng, W., An, Y., Shi, T., and Ma, D. (2009). High-throughput functional screening for autophagy-related genes and identification of TM9SF1 as an autophagosome-inducing gene. Autophagy *5*, 52–60.
15. Cauley, J.A., Robbins, J., Chen, Z., Cummings, S.R., Jackson, R.D., LaCroix, A.Z., LeBoff, M., Lewis, C.E., McGowan, J., Neuner, J., et al. (2003). Effects of estrogen plus progestin on risk of fracture and bone mineral density: the Women's Health Initiative randomized trial. JAMA *290*, 1729–1738.
16. Nollet, M., Santucci-Darmanin, S., Breuil, V., Al-Sahlanee, R., Cros, C., Topi, M., Momier, D., Samson, M., Pagnotta, S., Cailleteau, L., et al. (2014). Autophagy in osteoblasts is involved in mineralization and bone homeostasis. Autophagy *10*, 1965–1977.
17. Li, H., Li, D., Ma, Z., Qian, Z., Kang, X., Jin, X., Li, F., Wang, X., Chen, Q., Sun, H., and Wu, S. (2018). Defective autophagy in osteoblasts induces endoplasmic reticulum stress and causes remarkable bone loss. Autophagy *14*, 1726–1741.
18. Piemontese, M., Onal, M., Xiong, J., Han, L., Thostenson, J.D., Almeida, M., and O'Brien, C.A. (2016). Low bone mass and changes in the osteocyte network in mice lacking autophagy in the osteoblast lineage. Sci. Rep. *6*, 24262.
19. DeSelm, C.J., Miller, B.C., Zou, W., Beatty, W.L., van Meel, E., Takahata, Y., Klumperman, J., Tooze, S.A., Teitelbaum, S.L., and Virgin, H.W. (2011). Autophagy proteins regulate the secretory component of osteoclastic bone resorption. Dev. Cell *21*, 966–974.
20. Li, R.F., Chen, G., Ren, J.G., Zhang, W., Wu, Z.X., Liu, B., Zhao, Y., and Zhao, Y.F. (2014). The adaptor protein p62 is involved in RANKL-induced autophagy and osteoclastogenesis. J. Histochem. Cytochem. *62*, 879–888.
21. Zhang, L., Guo, Y.F., Liu, Y.Z., Liu, Y.J., Xiong, D.H., Liu, X.G., Wang, L., Yang, T.L., Lei, S.F., Guo, Y., et al. (2010). Pathway-based genome-wide association analysis identified the importance of regulation-of-autophagy pathway for ultradistal radius BMD. J. Bone Miner. Res. *25*, 1572–1580.
22. Glick, D., Barth, S., and Macleod, K.F. (2010). Autophagy: cellular and molecular mechanisms. J. Pathol. *221*, 3–12.
23. Bjørkøy, G., Lamark, T., Pankiv, S., Øvervatn, A., Brech, A., and Johansen, T. (2009). Monitoring autophagic degradation of p62/SQSTM1. Methods Enzymol. *452*, 181–197.
24. Tanida, I., Minematsu-Ikeguchi, N., Ueno, T., and Kominami, E. (2005). Lysosomal turnover, but not a cellular level, of endogenous LC3 is a marker for autophagy. Autophagy *1*, 84–91.
25. Laurin, N., Brown, J.P., Morissette, J., and Raymond, V. (2002). Recurrent mutation of the gene encoding sequestosome 1 (SQSTM1/p62) in Paget disease of bone. Am. J. Hum. Genet. *70*, 1582–1588.
26. Tong, X., Gu, J., Song, R., Wang, D., Sun, Z., Sui, C., Zhang, C., Liu, X., Bian, J., and Liu, Z. (2019). Osteoprotegerin inhibit osteoclast differentiation and bone resorption by enhancing autophagy via AMPK/mTOR/p70S6K signaling pathway in vitro. J. Cell. Biochem. *120*, 1630–1642.
27. Ma, J., Du, D., Liu, J., Guo, L., Li, Y., Chen, A., and Ye, T. (2020). Hydrogen sulphide promotes osteoclastogenesis by inhibiting autophagy through the PI3K/AKT/mTOR pathway. J. Drug Target. *28*, 176–185.
28. Camuzard, O., Santucci-Darmanin, S., Breuil, V., Cros, C., Gritsaenko, T., Pagnotta, S., Cailleteau, L., Battaglia, S., Panaïa-Ferrari, P., Heymann, D., et al. (2016). Sex-specific autophagy modulation in osteoblastic lineage: a critical function to counteract bone loss in female. Oncotarget *7*, 66416–66428.
29. Ma, Y., Qi, M., An, Y., Zhang, L., Yang, R., Doro, D.H., Liu, W., and Jin, Y. (2018). Autophagy controls mesenchymal stem cell properties and senescence during bone aging. Aging Cell *17*, e12709.
30. Mai, Q.G., Zhang, Z.M., Xu, S., Lu, M., Zhou, R.P., Zhao, L., Jia, C.H., Wen, Z.H., Jin, D.D., and Bai, X.C. (2011). Metformin stimulates osteoprotegerin and reduces RANKL expression in osteoblasts and

ovariectomized rats. J. Cell. Biochem. *112*, 2902–2909.

31. Ikeda, K., Ogawa, S., Tsukui, T., Horie-Inoue, K., Ouchi, Y., Kato, S., Muramatsu, M., and Inoue, S. (2004). Protein phosphatase 5 is a negative regulator of estrogen receptor-mediated transcription. Mol. Endocrinol. *18*, 1131–1143.
32. Schneider, C.A., Rasband, W.S., and Eliceiri, K.W. (2012). NIH Image to ImageJ: 25 years of image analysis. Nat. Methods *9*, 671–675.
33. Niwa, H., Araki, K., Kimura, S., Taniguchi, S., Wakasugi, S., and Yamamura, K. (1993). An efficient gene-trap method using poly A trap vectors and characterization of gene-trap events. J. Biochem. *113*, 343–349.
34. Kawai, S., Takagi, Y., Kaneko, S., and Kurosawa, T. (2011). Effect of three types of mixed anesthetic agents alternate to ketamine in mice. Exp. Anim. *60*, 481–487.
35. Nagai, S., Ikeda, K., Horie-Inoue, K., Shiba, S., Nagasawa, S., Takeda, S., and Inoue, S. (2016). Estrogen modulates exercise endurance along with mitochondrial uncoupling protein 3 downregulation in skeletal muscle of female mice. Biochem. Biophys. Res. Commun. *480*, 758–764.
36. Nishikawa, K., Nakashima, T., Takeda, S., Isogai, M., Hamada, M., Kimura, A., Kodama, T., Yamaguchi, A., Owen, M.J., Takahashi, S., and Takayanagi, H. (2010). Maf promotes osteoblast differentiation in mice by mediating the age-related switch in mesenchymal cell differentiation. J. Clin. Invest. *120*, 3455–3465.
37. Shah, F.A., Stoica, A., Cardemil, C., and Palmquist, A. (2018). Multiscale characterization of cortical bone composition, microstructure, and nanomechanical properties in experimentally induced osteoporosis. J. Biomed. Mater. Res. *106*, 997–1007.
38. Azuma, K., Ikeda, K., Suzuki, T., Aogi, K., Horie-Inoue, K., and Inoue, S. (2021). TRIM47 activates NF-κB signaling via PKC-ε/PKD3 stabilization and contributes to endocrine therapy resistance in breast cancer. Proc. Natl. Acad. Sci. USA *118*, e2100784118.
39. Livak, K.J., and Schmittgen, T.D. (2001). Analysis of relative gene expression data using real-time quantitative PCR and the 2(-Delta Delta C(T)) Method. Methods *25*, 402–408.
40. Azuma, K., Tanaka, M., Uekita, T., Inoue, S., Yokota, J., Ouchi, Y., and Sakai, R. (2005). Tyrosine phosphorylation of paxillin affects the metastatic potential of human osteosarcoma. Oncogene *24*, 4754–4764.

STAR★METHODS

KEY RESOURCES TABLE

REAGENT or RESOURCE	SOURCE	IDENTIFIER
Antibodies		
Mouse monoclonal anti-EBAG9	Ijichi et al.[10]	N/A
Rabbit polyclonal anti-TM9SF1	Aviva Systems Biology	Cat#APR44683; RRID: AB_938460
Rabbit anti-Mouse IgG HRP	Chemicon International	Cat#61-6520; RRID: AB_138451
Swine anti-Rabbit IgG HRP	DakoCytomation	Cat#P0399; RRID: AB_2617141
Mouse monoclonal anti-β-actin (clone AC-74)	Sigma-Aldrich	Cat#A5316; RRID: AB_476743
Rabbit polyclonal anti-p62/SQSTM1	Medical & Biological Laboratories	Cat#PM045; RRID: AB_1279301
Rabbit monoclonal anti-LC3B (clone D11)	Cell Signaling Technology	Cat#3868; RRID: AB_2137707
Sheep anti-Mouse IgG HRP	Cytiva	Cat#NA931; RRPI: AB_772210
Donkey anti-Rabbit IgG HRP	Cytiva	Cat#NA934; RRID: AB_772206
Chemicals, peptides, and recombinant proteins		
Medetnomidine hydrochloride (Domitor®)	Nippon Zenyaku Kogyo	N/A
Midazolam	Sandoz	N/A
Butorphanol (Vetorphale®)	Meiji Seika Pharma	N/A
17β-estradiol-3-benzoate	Sigma-Aldrich	Cat#E8515
Corn oil	Nacalai Tesque	Cat#25606-65
Collagenase	WAKO Pure Chemicals	Cat#032-22364
Dispase II	Roche	Cat#165859
Alpha minimum essential medium (α-MEM)	Nacalai Tesque	Cat#21445-95
Dulbecco's modified Eagle medium (DMEM)	Nacalai Tesque	Cat#08459-64
Penicillin-streptomycin solution	Fujifilm WAKO Pure Chemical	Cat#168-23191
ACK Lysing Buffer	Invitrogen	Cat#A1049201
Macrophage colony stimulating factor (M-CSF)	Peprotech	Cat#315-02
Soluble receptor activator of nuclear factor kappa-B ligand (sRANKL)	Oriental Yeast	Cat#47187000
β-glycerophosphate	Sigma-Aldrich	Cat#28-2840-2
L-ascorbic acid 2-phosphate	Nacalai Tesque	Cat#13570-66
Isoflurane	Fujifilm WAKO Pure Chemical	Cat#099-06571
Calcein	Dojin Chemical	Cat#C001
4% paraformaldehyde phosphate buffer solution	Fujifilm WAKO Pure Chemical	Cat#163-20145
Bovine serum albumin	Serologicals Proteins	
3,3′-Diaminobenzidine tetrahydrochloride (DAB)	Dojin Chemical	Cat#D006
Epoxy resin	Taab	Epon 812
Arizarin red solution	PG Research	Cat#ARD-A1
5% silver nitrate solution	ScyTek Laboratories	Cat#SNV125
5% sodium thiosulfate solution	ScyTek Laboratories	Cat#STB125
Pepstatin A	Peptide Institute	Cat#4397
E64d	Tokyo Chemical Industry	Cat#E1337
Critical commercial assays		
Three-point bending test of bones	Hamri	https://hamuri.co.jp
ELISA Kit for Procollagen I N-terminal Propeptide (PINP)	Cloud-Clone	Cat#SEA957Mu

(*Continued on next page*)

Continued

REAGENT or RESOURCE	SOURCE	IDENTIFIER
RatLaps® Collagen I ELISA Kit	Immunodiagnostic Systems	Cat#AC-06F1
Alkaline phosphatase staining Kit	Cosmo Bio	Cat#AK20
TRAP staining Kit	Cosmo Bio	Cat#AK04F
Bone resorption assay plate (48 well)	PG Research	Cat#BRA-48P
Sepasol®-RNA I Super G	Nacalai Tesque	Cat#09379-97
PrimeScript® RT reagent Kit	Takara	Cat#RR037A
KAPA SYBR Fast qPCR Kit	Kapa Biosystems	Cat#KK4600
Adenovirus Expression Vector Kit	Takara	Cat#6170
Lipofectamine RNAiMAX	Thermo Fisher Scientific	Cat#13778150
Proteinase inhibitor cocktail	Nacalai Tesque	Cat#03969-21
Polyvinylidene difluoride (PVDF) membrane (Immobilon-P)	Millipore	Cat#IPVH00010
Bullet Blocking One	Nacalai Tesque	Cat#13779-01
Chemilumi-One Ultra	Nacalai Tesque	Cat#11644
WB Stripping solution	Fujifilm WAKO Pure Chemical	Cat#193-16375
Experimental models: Cell lines		
Mouse: MC3T3-E1 cells subclone 4	ATCC	CRL-2593
Mouse: RAW264.7 cells	ATCC	TIB-71
Experimental models: Organisms/strains		
C57BL/6NJcl	CREA Japan	N/A
Ebag9-knockout mice (C57BL/6NJcl)	Miyazaki et al.[12]	N/A
Oligonucleotides		
Primer: *Sry* forward: 5′- CCATGTCAAGCGCCCCATGA-3′	This paper	N/A
Primer: *Sry* reverse: 5′- GTAAGGCTTTTCCACCTGCA -3′	This paper	N/A
Primer: *Gapdh* forward: 5′- GCATGGCCTTCCGTGTTC -3′	This paper	N/A
Primer: *Gapdh* reverse: 5′- TGTCATCATACTTGGCAGGTTTCT -3′	This paper	N/A
Primer: *Ebag9* forward: 5′- GCAACAGTGTTCTCGTTCCT -3′	This paper	N/A
Primer: *Ebag9* reverse: 5′- TGGGCAAAGTTATTTGATCTCC -3′	This paper	N/A
Primer: *Alp* forward: 5′- CCAATGTAGCCAAGAATGTCATCA -3′	This paper	N/A
Primer: *Alp* reverse: 5′- GATTCGGGCAGCGGTTACT -3′	This paper	N/A
Primer: *Tm9sf1* forward: 5′- ATCTTGTTGTATGCCCTGACC -3′	This paper	N/A
Primer: *Tm9sf1* reverse: 5′- AGTTCACCACACTCCAAGTC -3′	This paper	N/A
Primer: *Ctsk* forward: 5′- GCTATATGACCACTGCCTTCC -3′	This paper	N/A
Primer: *Ctsk* reverse: 5′- ATTTAGCTGCCTTTGCCGTG -3′	This paper	N/A
siControl Sense: 5′- GUGGAUUUCGAGUCGUCUUAA -3′ Anti-sense: 5′- AAGACGACUCGAAAUC CACAU -3′	This paper	N/A
siEbag9 #1 Sense: 5′- GCCCACUACAGUUGAUUAUUC -3′ Anti-sense: 5′- AUAAUCAACUGUAGUGGGCAA -3′	This paper	N/A
siEbag9 #2 Sense: 5′- GGUAGCACGGGUUUUUCCAGU -3′ Anti-sense: 5′- UGGAAAAACCCGUGCUACCAU -3′	This paper	N/A
siTm9sf1 #1 Sense: 5′- UUCAAAUAUAUAUAUUCCUU -3′ Anti-sense: 5′- GGAAUAUAUAUAUUUGAACUU -3′	This paper	N/A

(*Continued on next page*)

Continued

REAGENT or RESOURCE	SOURCE	IDENTIFIER
siTm9sf1 #2 Sense: 5′- AUUUUCCAGCCAUUAUCGCCC -3′ Anti-sense: 5′- GCGAUAAUGGCUGGAAAAUUA -3′	This paper	N/A
Recombinant DNA		
pEGFP-C2	Clontech	Cat#6083-1
pDsRed-N1	Clontech	Cat#632469
pcDNA3	Invitrogen	N/A
LC3B-pEGFP	This paper	N/A
EBAG9-pDsRed-N1	Miyazaki et al.[13]	N/A
Flag-EBAG9-pcDNA3	Miyazaki et al.[13]	N/A
HA-TM9SF1-pcDNA3	Miyazaki et al.[13]	N/A
Adeno-EBAG9	This paper	N/A
Adeno-GFP	Ikeda et al.[31]	N/A
CellLignt® Golgi-GFP BacMam 2.0	Thermo Fisher Scientific	Cat#C10593
Software and algorithms		
ImageJ	Schneider et al.[32]	https://imagej.nih.gov/ij/
GraphPad Prism 8.4.3	GraphPad Software	https://www.graphpad.com
SkyScan NRecon	Micro Photonics	https://www.microphotonics.com/micro-ct-systems/nrecon-reconstruction-software/
Analyze 12.0	AnalyzeDirect	https://analyzedirect.com
Other		
Densitometer	GE medical Systems	PIXImus2
Material testing machine	Maruto	MZ500S
Micro-computed tomography	Bruker	SkyScan 1176, SkyScan 1276
Micro-computed tomography	Rigaku	CosmoScan GX
Microtome	Ivan Sorvall	Sorvall MT-5000
Transmission electron microscope	Hitachi	H-7100
Real-time PCR system	Applied Biosystems	7500 Fast
Real-time PCR system	Applied Biosystems	StepOne Plus
Confocal fluorescence microscopy	Olympus	Fluoview 10i

RESOURCE AVAILABILITY

Lead contact

Further information and requests for resources and reagents should be directed to and will be fulfilled by the lead contact, Satoshi Inoue (sinoue@tmig.or.jp).

Materials availability

Plasmids generated in this study are available from the lead contact upon request.

This study did not generate new unique reagents.

Date and code availability

- All data reported in this paper will be shared by the lead contact upon request.
- This paper does not report original code.
- Any additional information required to reanalyze the data reported in this paper is available from the lead contact upon request.

EXPERIMENTAL MODEL AND STUDY PARTICIPANT DETAILS

Generation of *Ebag9*-knockout mice

Generation of *Ebag9*-knockout mice was described previously.[12] Briefly, we first generated *Ebag9* floxed mice in which two loxP sequences are inserted into the both adjacent introns of the 2nd exon of *Ebag9* gene containing the translation initiation codon. Then, the *Ebag9* floxed mice were crossed with Ayu1-Cre mice in which Cre recombinase is expressed from the early stage of embryogenesis in ES cells.[33] *Ebag9*-knockout mice were generated when the exon 2 of *Ebag9* was floxed in the germline cells. *Ebag9*-knockout mice were maintained in the C57BL/6NJcl background. Wild-type C57BL/6NJcl mice were used as control mice.

Animal experiments

Male and female *Ebag9*-knockout and wild-type mice were used for experiments. The age and sex of the mice in each experiment is indicated in the main text and figure legends. Mice were housed in a temperature-controlled room (22°C) with a 12-hour light/dark schedule, had free access to water, and were fed standard laboratory chow. When ovariectomy was performed, mice were anesthesized with a mixure of 0.75 mg/kg medetomidine hydrochloride (Domitor, Nippon Zenyaku Kogyo, Fukushima, Japan), 4 mg/kg midazolam (Sandoz, Holzkirchen, Germany), and 5 mg/kg butorphanol (Vetorphale, Meiji Seika Pharma, Tokyo, Japan).[34] In sham operation, same procedure was performed except excision of ovaries. Two weeks after surgeries, cyclic estrogen or ethanol vehicle treatment was started. Namely, ovariectomized mice were injected subcutaneously with 10 μg/kg 17β-estradiol-3-benzoate (Sigma-Aldrich) or control ethanol vehicle, respectively, in 100 ml corn oil (Nacalai tesque), and sham-operated mice were administered with control ethanol vehicle in 100 ml corn oil twice a week for 4 weeks before sacrifice.[35] All experimental procedures using laboratory animals were approved by the Animal Care and Use Committee of Tokyo Metropolitan Institute for Geriatrics and Gerontology (TMIG) (Approval Number: 180023) and were in accordance with the guidelines for the Care and Use of Laboratory Animals of TMIG.

Isolation of primary osteoblasts

Primary osteoblasts were isolated from calvariae of 1 or 2-day-old mice. The sex of the mouse was confirmed by DNA isolated from the tail of the mouse with PCR reaction using primers targeting *Sry* gene. Sequences of primers are as follows.

Sry forward: 5′- CCATGTCAAGCGCCCCATGA -3′

Sry reverse: 5′- GTAAGGCTTTTCCACCTGCA -3′

The sex of the primary osteoblasts in each experiment is indicated in the main text and the figure legends. After removal of soft tissue, the calvariae were digested with 1 mg/mL collagenase (Fujifilm WAKO Pure Chemical Industries) and 2 mg/mL dispase (Roche, Mannheim, Germany) in PBS for 1 h at 37°C. The cells migrating from the calvariae were collected and grown in α-MEM (Nacalai Tesque, Kyoto, Japan) with 10% FBS and 1% penicillin-streptomycin (Fujifilm Wako Pure Chemical Industries) at 37°C with 5% CO_2.

Isolation of primary osteoclast precursors

Bone marrow cells from femoral and tibial bones of mice were treated with ACK Lysing Buffer (Invitrogen, Carlsbad, CA, USA) for 5 min. The age and sex of the mice in each experiment is indicated in the main text and figure legends. The bone marrow cells were subsequently cultured in α-MEM containing 10% FBS, 1% penicillin-streptomycin and 10 ng/ml macrophage colony-stimulating factor (M-CSF) (PeproTech, Rocky Hill, NJ, USA) for 1 day. Nonadherent cells were harvested and cultured for three more days in the presence of 30 ng/ml M-CSF. Floating cells were removed, and adherent cells were used as osteoclast precursors (bone marrow macrophages; BMM).

Cell culture

Murine calvaria-derived preosteoblastic cell line MC3T3-E1 subclone 4 and murine macrophage cell line RAW264.7 were obtained from ATCC (Manassas, VA, USA). MC3T3-E1 cells, primary osteoblasts, and primary osteoclast precursors were cultured in α-MEM with 10% FBS and 1% penicillin-streptomycin at 37°C with 5% CO_2. RAW264.7 cells were cultured in Dulbecco's modified Eagle's medium (DMEM) (Nacalai Tesque) with 10% FBS and 1% penicillin-streptomycin at 37°C with 5% CO_2.

Osteogenic differentiation

For osteogenic differentiation, primary osteoblasts or MC3T3-E1 cells were cultured in α-MEM containing 10% FBS, 1% penicillin-streptomycin, β-glycerophosphate (Sigma-Aldrich, St Louis, MO, USA) (10 mM) and L-ascorbic acid 2-phosphate (Nacalai Tesque) (0.2 mM). The sex of the primary osteoblasts in each experiment is indicated in the main text and the figure legends.

Osteoclastic differentiation

For osteoclastic differentiation, osteoclast precursor cells derived from female mice were cultured in α-MEM containing 10% FBS, 1% penicillin-streptomycin, 10 ng/ml macrophage colony-stimulating factor (M-CSF), and 100 ng/ml recombinant human soluble receptor activator of nuclear factor kappa-B ligand (sRANKL) (Oriental Yeast, Tokyo, Japan). For osteoclastic differentiation of RAW264.7 cells, the cells were cultured with DMEM containing 10% FBS, 1% penicillin-streptomycin, and 100 ng/ml or 150 ng/ml sRANKL.

METHOD DETAILS

Bone mineral density (BMD) measurements

The BMD of the femoral bones was measured by dual-energy X-ray absorptiometry (DXA) using the Lunar PIXImus2 densitometer (GE Medical Systems, Madison, WI, USA). The whole leg was fixed with 70% ethanol and placed in a specimen tray. After calibration, duplicate cycles of four scans were obtained. The region of the femoral bone was selected and analyzed.

Three-point bending test

The mechanical properties of the diaphysis of femoral bones were evaluated by a three-point bending test carried out at the laboratory of Hamri (Ibaraki, Japan). A load was applied midway between two supports that were placed 8mm apart. The femur was positioned so that the loading point was at the center of the femoral diaphysis and bending occurred in the medial-lateral axis. The bending test was carried out in a saline bath at 37°C. Load displacement curves were recorded at a crosshead speed of 5mm/min using a material testing machine MZ500S (Maruto Co., Ltd.,Tokyo, Japan). The peak load and stiffness were analyzed using CTRwin software (System Supply Co., Ltd., Kanagawa, Japan).

Quantitative micro-computed tomography

For quantitative micro-CT analysis, mice were temporarily anaesthetized with isoflurane (Fujifilm WAKO Pure Chemical Industries, Osaka, Japan) during examination, and their femurs were analyzed using a micro-computed tomography (micro-CT) system SkyScan 1176 or 1276 (Bruker, Kontich, Belgium) operating with a detection pixel size of 7.5 μm. Images were reconstructed using SkyScan NRecon software (Bruker). In the experiment of 3-month-old mice, CosmoScan GX (Rigaku, Tokyo, Japan) was used as a micro-CT with a pixel size of 9 μm for trabecular bones or 15 μm for cortical bones, and the images were reconstructed using Analyze 12.0 (AnalyzeDirect, Inc., KS, USA). Trabecular bone analysis was performed at a region 0.8–1.8 mm above the distal growth plate of femur.[36] Cortical bone analysis was performed at the diaphysis of femur 4-5 mm above the distal growth plate.[37]

Bone histomorphometry

Mice were injected with 20 mg/kg calcein (Dojin Chemical, Kumamoto, Japan) subcutaneously 5 and 2 days before sacrifice. The mice were euthanized 2 days after last calcein injection, and their legs were dissected for bone histomorphometric analysis. After soft tissues were removed, the tibial bones were fixed with 4% paraformaldehyde phosphate buffer solution (Fujifilm Wako Pure Chemical Industries). Five-micrometer-thick coronal specimens of the proximal tibia were used for bone histomorphometry. The border of primary or secondary spongiosa was defined by diffuse or clear calcein labels recognized by fluorescent scope. The region of the secondary spongiosa, within 100 to 1100 μm distal to the growth plate, and exclusion of one cortex thick from both lateral and medical cortexes, was measured.

Bone immunohistochemistry

Femoral bones were decalcified with 10% EDTA-2Na and dehydrated in ascending ethanol solutions prior to paraffin embedding and sectioning. Dewaxed paraffin sections were examined for EBAG9 and TM9SF1. In brief, after inhibition of endogenous peroxidases with methanol containing 0.3% hydrogen peroxidase for 30 min, dewaxed paraffin sections were pretreated with 1% bovine serum albumin (BSA; Serologicals Proteins Inc., Kankakee, IL, USA) in PBS (1% BSA-PBS) for 30 min. Sections were then incubated for 2-3 h at room temperature (RT) with mouse monoclonal EBAG9 antibody diluted at 1:100 with 1% BSA-PBS or rabbit polyclonal TM9SF1 antibody (APR44683, AVIVA SYSTEMS BIOLOGY, San Diego, CA, USA) diluted at 1:100. They were followed by incubation with horseradish (HRP)-conjugated anti-mouse IgG (61-6520, Chemicon International Inc., Temecula, CA, USA) or HRP-conjugated anti-rabbit IgG (P0399, DakoCytomation, Glostrup, Denmark). For visualization of all HRP-conjugated immunoreactions, diaminobenzidine tetrahydrochloride (DAB) (Dojin chemical) was employed as a substrate.

Transmission electron microscopic (TEM) analysis

For TEM analysis, anesthesia was performed with a mixure of 0.75 mg/kg medetomidine hydrochloride (Domitor, Nippon Zenyaku), 4 mg/kg midazolam (Sandoz), and 5 mg/kg butorphanol (Vetorphale, Meiji Seika Pharma).[34] Subsequently, perfusion was performed with 4% paraformaldehyde in 0.1 M cacodylate buffer (pH 7.4) through the cardiac left ventricle. Femoral bones were removed and immersed in the same fixative for additional 12 h at 4°C. Non-decalcified specimens destined for transmission electron microscopic (TEM) observations were post-fixed with 1% OsO_4 in 0.1 M cacodylate buffer (pH 7.4) for 4 h at 4°C, dehydrated with ascending concentrations of acetone and embedded in epoxy resin (Epon 812; Taab, Berkshire, UK). Ultrathin sections from non-decalcified samples obtained with the use of a microtome (Sorvall MT-5000; Ivan Sorvall, Inc., Norwalk, CT, USA). The diamond knife's boat was filled with ethylene glycol to permit the collection of the sections without dissolution of calcium phosphates. TEM observation (Hitachi H-7100, Hitachi Co. Ltd, Tokyo, Japan) was conducted at 80 kV. Nucleus-to-cytoplasm ratio of osteocytes were analyzed by Image J software (US National Institutes of Health, Bethesda, MD, USA).[32]

Enzyme-linked immunosorbent assay (ELISA)

The serum concentrations of procollagen I N-terminal propeptide (PINP) and cross-linked C-terminal telopeptide of type I collagen (CTX-I) were measured using PINP ELISA Kit (Cloud-Clone, Huston, U.S.A.) and RatLaps CTX-I EIA assay (Immunodiagnostic Systems, Frankfurt am Mein, Germany) respectively according to the manufacturers' instruction.

Antibodies and reagents

Mouse monoclonal EBAG9 antibody was generated against a glutathione S-transferase–EBAG9 fusion protein as previously described.[10] Mouse monoclonal β-actin antibody (clone: AC-74) was purchased from Sigma (St. Louis, MO, USA). Rabbit polyclonal p62(SQSTM1) antibody (PM045) was purchased from Medical & Biological Laboratories (Nagoya, Japan). Rabbit monoclonal antibody for microtubule-associated protein 1 light chain 3 beta (LC3B) (clone: D11) was obtained from Cell Signaling Technology (Beverly, MA, USA). Rabbit polyclonal TM9SF1 antibody was purchased from AVIVA SYSTEMS BIOLOGY (San Diego, CA, USA). Pepstatin A was purchased from Peptide Institute (Osaka, Japan) and E64d was purchased from Tokyo Chemical Industry (Tokyo, Japan).

Evaluation of alkaline phosphatase activity

Osteoblastic cells were fixed with 10% formalin neutral buffer for 20 min. Subsequently, the alkaline phosphatase activity in osteoblastic cells was evaluated by staining cells with an alkaline phosphatase staining kit (Cosmo Bio, Tokyo, Japan). Stained area was quantified using Image J software (US National Institutes of Health).[32] The relative stained area was calculated by dividing with the evaluated area.

Alizarin red staining

Osteoblastic cells were fixed with 10% formalin neutral buffer for 20 min. Subsequently, the cells were stained with alizarin red solution (PG Research, Tokyo, Japan) for 30 min at room temperature. Stained area was quantified using Image J software (US National Institutes of Health).[32] The relative stained area was calculated by dividing with the evaluated area.

Von Kossa staining

Osteoblastic cells were incubated with 5% silver nitrate solution (ScyTek Laboratories, Logan, UT, USA) under ultraviolet light for 30 min. Subsequently, the cells were treated with 5% sodium thiosulfate solution (ScyTek Laboratories) for 2 min. Stained area was quantified using Image J software (US National Institutes of Health).[32] The relative stained area was calculated by dividing with the evaluated area.

TRAP staining

After primary osteoclastic precursor cells or RAW264.7 cells were fixed in 10% formalin neutral buffer for 5 min and stained with tartrate-resistant acid phosphatase (TRAP) using a TRAP staining kit (Cosmo Bio).

Pit formation assay

Pit formation assays were performed using bone resorption assay plate (PG Research) coated with calcium phosphate. RAW264.7 cells were cultured in differentiation medium. To evaluate pit area, cells were removed by 5% sodium hypochlorite and photographs of five randomly selected fields were taken under a microscope at a magnification of ×80. Resorbed area was quantified using Image J software (US National Institutes of Health).[32] The relative area of resorbing lacunae is expressed as the percent of the area to the entire field.

Quantitative reverse transcription polymerase chain reaction

Quantitative reverse transcription polymerase chain reaction (qRT-PCR) was performed as previously described.[38] Briefly, total RNAs were extracted using Sepasol-RNA I Super G (Nacalai Tesque) followed by cDNA synthesis using PrimeScript (Takara, Kyoto, Japan). The cDNA was subjected to real-time polymerase chain reaction (PCR) using 7500Fast real time PCR system or StepOne Plus real time PCR system (Applied Biosystems, Foster City, CA, USA) based on detection of SYBR Green fluorescence (Kapa Biosystems, Woburn, MA, USA). Mean Ct values were normalized to *Gapdh*, and relative mRNA levels were then calculated by using the $2^{-\Delta\Delta C}{}_{T}$ method[39] with relative gene expression presented as mean over control. Sequences of primers are as follows.

Gapdh forward: 5′- GCATGGCCTTCCGTGTTC -3′
Gapdh reverse: 5′- TGTCATCATACTTGGCAGGTTTCT -3′
Ebag9 forward: 5′- GCAACAGTGTTCTCGTTCCT -3′
Ebag9 reverse: 5′- TGGGCAAAGTTATTTGATCTCC -3′
Alp forward: 5′- CCAATGTAGCCAAGAATGTCATCA -3′
Alp reverse: 5′- GATTCGGGCAGCGGTTACT -3′
Tm9sf1 forward: 5′- ATCTTGTTGTATGCCCTGACC -3′
Tm9sf1 reverse: 5′- AGTTCACCACACTCCAAGTC -3′
Ctsk forward: 5′- GCTATATGACCACTGCCTTCC -3′
Ctsk reverse: 5′- ATTTAGCTGCCTTTGCCGTG -3′

Plasmid construction and transfection

EGFP-linked human microtubule-associated protein 1 light chain 3 beta (EGFP-hLC3B) plasmid was constructed by subcloning cDNA encoding human LC3B into pEGFP-C2 expression vector (Clontech, Palo Alto, CA, USA) using Xho I and EcoRI restriction sites. DsRed-linked human EBAG9 (EBAG9-DsRed) plasmid, Flag-tagged human EBAG9 plasmid, and Flag tagged human TM9SF1 plasmid were constructed as previously described.[13] Transfection of expression vectors was performed 24 h after seeding the cells using FuGENE HD (Promega, Madison, WI, USA) according to the manufacturer's instructions. Recombinant adenoviruses expressing EBAG9 (Ad-EBAG9) and green fluorescent protein (Ad-GFP) as control were prepared using Adenovirus Expression Vector Kit (Takara Bio Inc., Shiga, Japan).[31] They were infected at a multiplicity of infection (MOI) of 3.

Fluorescence microscopy imaging

Fluorescent images of the cells expressing proteins linked with fluorophores were visualized with confocal fluorescence microscopy, Fluoview 10i (Olympus, Tokyo, Japan). Localization in the Golgi apparatus was visualized with CellLight Golgi-GFP BacMam 2.0 (Thermo Fisher Scientific, Waltham, MA) according to the manufacturer's instructions.

Small interfering RNA transfection

Silencing of *Ebag9* or *Tm9sf1* was performed by small interfering RNA (siRNA) transfection. Two specific siRNAs targeting each gene, and a control siRNA targeting firefly luciferase (siControl), were purchased from RNAi Inc (Tokyo, Japan). When these siRNAs were transfected to MC3T3-E1 cells, they were transfected at the time of seeding cells by reverse transfection method. When siRNAs were transfected to RAW264.7 cells, they were transfected on the next day of seeding cells by forward transfection method. Lipofectamine RNAiMAX (Thermo Fisher Scientific, St. Louis, MO, USA) was used for transfecting siRNAs according to the manufacturer's instructions. The sequences of siRNA were as follows.

siControl
Sense: 5′- GUGGAUUUCGAGUCGUCUUAA -3′
Anti-sense: 5′- AAGACGACUCGAAAUCCACAU -3′ siEbag9 #1 Sense: 5′- GCCCACUACAGUUGAUUAUUC -3′
Anti-sense: 5′- AUAAUCAACUGUAGUGGGCAA -3′ siEbag9 #2 Sense: 5′- GGUAGCACGGGUUUUUCCAGU -3′
Anti-sense: 5′- UGGAAAAACCCGUGCUACCAU -3′
siTm9sf1 #1
Sense: 5′- UUCAAAUAUAUAUAUUCCUU -3′
Anti-sense: 5′- GGAAUAUAUAUAUUUGAACUU -3′
siTm9sf1 #2
Sense: 5′- AUUUUCCAGCCAUUAUCGCCC -3′
Anti-sense: 5′- GCGAUAAUGGCUGGAAAAUUA -3′

Western blot analysis

Western blot analysis was performed as previously described[40] with some modifications. Cells were lysed using a lysis buffer containing 50 mM 4-(2-hydroxyethyl)-1-piperazinyl-ethane-2-sulfonic acid (HEPES), 150 mM NaCl, 10% glycerol, 1% Triton X-100, 1.5 mM $MgCl_2$, and 1 mM ethylene glycol-bis-(β-amino-ethyl ether) N, N, N′, N′-tetra-acetic acid (EGTA). A proteinase inhibitor cocktail (Nacalai Tesque, Kyoto, Japan) was added before use. When autophagy was evaluated, cells were treated with pepstatin A (10 μg/mL) and E64d (10 μg/mL) for 4 to 5 h before cell lysis.[23] Cell lysates were separated on sodium dodecyl sulfate polyacrylamide gel electrophoresis (SDS-PAGE), and then transferred to polyvinylidene difluoride (PVDF) membranes (Millipore, Darmstadt, Germany). The membranes were blocked in Bullet Blocking One (Nacalai Tesque) for 5 min. The membranes were incubated with primary antibodies, followed by incubation with horseradish peroxidase (HRP)-conjugated secondary antibody (GE Healthcare, Buckinghamshire, UK). The bound antibodies were visualized with Chemilumi-One Ultra (Nakalai Tesque). In case of re-probing, the antibodies were stripped using WB Stripping Solution (Fujifilm Wako Pure Chemical Industries).

QUANTIFICATION AND STATISTICAL ANALYSIS

Nuclear area and cytoplasmic area of the osteocytes in the transmission electron microscopic analysis, stained area of the primary osteoblasts and the osteoblastic cells in the differentiation assays, and resorbed area in the pit formation assay were quantified using Image J software (US National Institutes of Health).[32] Statistical analyses were conducted using GraphPad Prism 8.4.3 (GraphPad Software, San Diego, CA USA). The statistical analyses were performed using Student's t-test, one-way ANOVA followed by Dunnett's test as a post-hoc analysis, or two-way ANOVA.